Magnetocrystalline anisotropy and magnetization reversal in $Ga_{1-x}Mn_xP$ synthesized by ion implantation and pulsed-laser melting

C. Bihler,* M. Kraus, H. Huebl, and M. S. Brandt
Walter Schottky Institut, Technische Universität München, Am Coulombwall 3, 85748 Garching, Germany

S. T. B. Goennenwein and M. Opel
Walther-Meissner-Institut, Bayerische Akademie der Wissenschaften, Walther-Meissner-Strasse 8, 85748 Garching, Germany

M. A. Scarpulla,† P. R. Stone, R. Farshchi, and O. D. Dubon
Department of Materials Science and Engineering, University of California, Berkeley and Lawrence Berkeley National Laboratory, Berkeley, California 94720, USA

(Received 22 March 2007; published 18 June 2007)

We report the observation of ferromagnetic resonance (FMR) and the determination of the magnetocrystalline anisotropy in (100)-oriented single-crystalline thin film samples of $Ga_{1-x}Mn_xP$ with $x=0.042$. The contributions to the magnetic anisotropy were determined by measuring the angular and the temperature dependencies of the FMR resonance fields and by superconducting quantum interference device magnetometry. The largest contribution to the anisotropy is a uniaxial component perpendicular to the film plane; however, a negative contribution from cubic anisotropy is also found. Additional in-plane uniaxial components are observed at low temperatures, which lift the degeneracy between the in-plane [011] and [01$\bar{1}$] directions as well as between the in-plane [010] and [001] directions. Near $T=5$ K, the easy magnetization axis is close to the in-plane [01$\bar{1}$] direction. All anisotropy parameters decrease with increasing temperature and disappear above the Curie temperature T_C. A consistent picture of the magnetic anisotropy of ferromagnetic $Ga_{1-x}Mn_xP$ emerges from the FMR and magnetometry data. The latter can be successfully modeled when both coherent magnetization rotation and magnetic domain nucleation are considered.

DOI: 10.1103/PhysRevB.75.214419 PACS number(s): 75.30.Gw, 75.50.Pp, 76.50.+g

I. INTRODUCTION

Mn-based diluted magnetic semiconductors show a variety of different magnetic ordering phenomena ranging from ferromagnetism mediated by quasidelocalized holes in materials exhibiting metallic conductivity[1,2] to spin-glass-like behavior in semiconducting matrices attributed to Mn-rich nanoclusters.[3] An important parameter expected to govern the magnetic ordering is the localization of the charge carriers coupling the 3*d* high-spin states commonly introduced by Mn incorporation. In III-V materials, where Mn simultaneously acts as acceptor, the corresponding acceptor level essentially determines the degree of localization of the holes.[4] A variation of the acceptor level can be achieved by changing the group-V atom in III-V alloys. While recent studies on $Ga_{1-x}Mn_xN$ indicate the formation of a ferromagnetic ordering in essentially insulating material with a Curie temperature T_C of 8 K,[5] a carrier-mediated, nonmetallic phase with T_C up to 65 K in $Ga_{1-x}Mn_xP$ has recently been synthesized.[6–9] In this material, it was shown that T_C increases with the magnetic dopant concentration and that ferromagnetism is suppressed by the addition of compensating Te (Ref. 6) and S donors.[8] Furthermore, x-ray absorption spectroscopy and x-ray magnetic circular dichroism have indicated that the local ferromagnetic environment for Mn in $Ga_{1-x}Mn_xP$ is very similar to that in $Ga_{1-x}Mn_xAs$ and that the Mn *d*-derived density of states at E_F is strongly spin polarized.[9]

In $Ga_{1-x}Mn_xAs$, the magnetocrystalline anisotropy has been successfully described in terms of the GaAs valence band because the states occupied by holes mediating inter-Mn exchange appear to be sufficiently similar to the unperturbed GaAs valence band.[10] It has been previously pointed out[11,12] that the holes responsible for exchange mediation are probably at least semilocalized in real space, as assumed in polaronic theories[13,14] also used to describe diluted magnetic semiconductors. Evidence for some degree of hole localization in III-Mn-V ferromagnetic semiconductors has been observed in infrared studies of low-temperature molecular beam epitaxy (LT-MBE) grown $In_{1-x}Mn_xAs$ (Ref. 15)

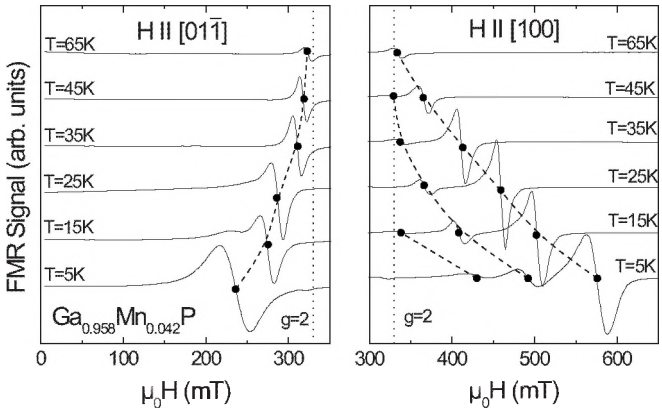

FIG. 1. Temperature dependence of the FMR signal of a $Ga_{0.958}Mn_{0.042}P$ sample for the magnetic field aligned along the in-plane [01$\bar{1}$] (left panel) and the out-of-plane [100] (right panel) directions. The dashed lines are guides to the eye. The magnetic field corresponding to $g=2$ is indicated by dotted vertical lines.

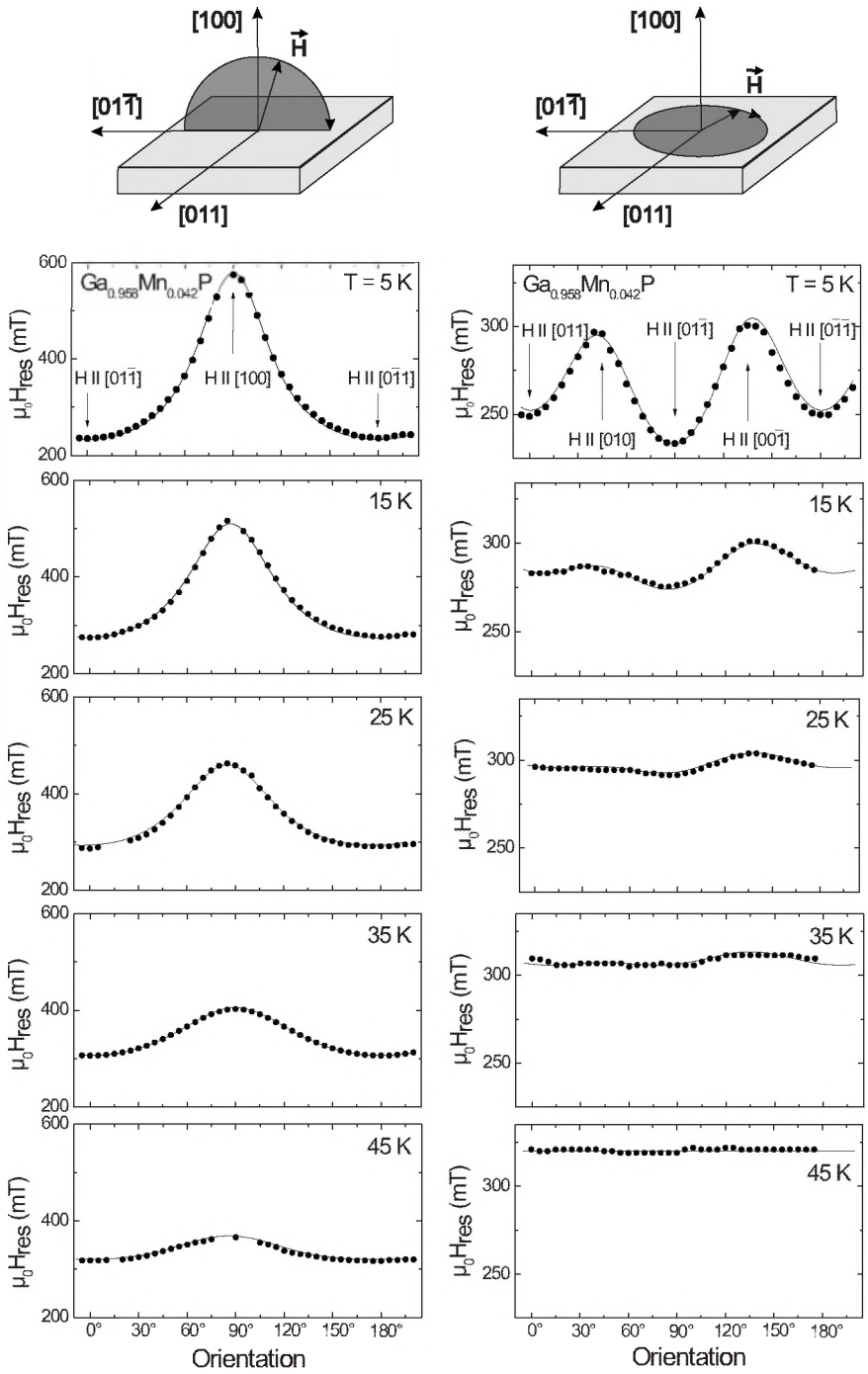

FIG. 2. Angular dependence of the ferromagnetic resonance fields for the magnetic field rotating within the (011) (left panels) and (100) (right panels) planes at T =5, 15, 25, 35, and 45 K. The circles correspond to the experimentally observed resonance positions. The full lines show the anisotropy expected for the parameters shown in Fig. 4.

and $Ga_{1-x}Mn_xAs$.[16] In these materials it is believed that there is significant mixing between the valence and Mn impurity bands, while our studies in $Ga_{1-x}Mn_xP$ suggest that the exchange-mediating holes reside in a separate Mn impurity band.[6–8] Conduction in this band occurs by hopping in the ferromagnetic regime, indicating a much higher degree of localization than in $Ga_{1-x}Mn_xAs$ or $In_{1-x}Mn_xAs$.[7] This suggests that, as predicted by *ab initio* calculations,[17–21] a discontinuous transition to an alternative mechanism of carrier-mediated exchange does not occur even with these distinctions in band structure. As the magnetic anisotropy is intimately tied to the properties of the exchange-mediating holes, it is important to investigate the magnetic anisotropy connected with the impurity band in $Ga_{1-x}Mn_xP$. Therefore, after giving a short introduction into the sample fabrication and the measurement techniques in Sec. II, we determine the contributions to the magnetic anisotropy of $Ga_{1-x}Mn_xP$ by measuring the angular- and the temperature-dependence of ferromagnetic resonance (FMR) fields in Sec. III. The FMR results are substantiated by superconducting quantum interference device (SQUID) magnetization measurements in Sec. IV.

II. EXPERIMENTAL

Samples were prepared by ion implantation followed by pulsed-laser melting (II-PLM).[22,23] For the present study, un-

intentionally sulfur-doped n-type GaP (100) wafers with a carrier concentration in the range of $10^{16}-10^{17}$ cm^{-3} were implanted with 50 keV Mn ions. Each implanted sample was cleaved to have $[01\bar{1}]$ and [011] edges and was irradiated in air with a single 0.4 J cm^{-2} pulse (FWHM=23 ns) from a KrF excimer laser (λ=248 nm) homogenized to a spatial uniformity of ±5% by a crossed-cylindrical lens homogenizer. Channeling $^4He^+$ Rutherford backscattering spectrometry (RBS) and particle induced x-ray emission (PIXE) were used to assess the crystalline quality, Mn dose retained after II-PLM, and substitutional fraction of Mn in the samples.[23] Once processed the films are high-quality single crystals with a Mn dose of 7.3×10^{15} cm^{-2} and substitutionality of 0.7, i.e., 70% of Mn atoms substitute Ga atoms. We note that the remaining 30% of Mn atoms do not form interstitial defects and instead are incommensurate with the GaAs lattice presumably in the form of small clusters. This level of substitutionality is not unlike $Ga_{1-x}Mn_xAs$ films of higher Mn concentration grown by low-temperature molecular beam epitaxy, which contain on the order of 20% nonsubstitutional Mn.[24]

II-PLM processing results in samples having a gradient in Mn concentration into the depth of the sample as measured by secondary ion mass spectrometry (SIMS), making it impossible to determine single values for the film thickness and Mn concentration. The Mn SIMS profile can be approximated by a Gaussian distribution centered at a depth of 40 nm with a width of 20 nm. However, as the regions of the film with highest Mn concentration dominate both the magnetic and transport properties, samples are discussed here in terms of their peak *substitutional* Mn concentration, which was determined by channeling RBS and PIXE to be $x=0.042$.[6,7] Sample magnetization was determined in various crystallographic orientations using a superconducting quantum interference device (SQUID) magnetometer. The FMR measurements were performed at $\omega/2\pi\approx9.3$ GHz in an electron paramagnetic resonance (EPR) spectrometer using magnetic field modulation, with the sample temperature controlled using a liquid-He flow cryostat.

III. FERROMAGNETIC RESONANCE SPECTROSCOPY

The left panel of Fig. 1 shows the temperature dependence of the FMR signal of a typical $x=0.042$ sample for the magnetic field aligned along the in-plane $[01\bar{1}]$ direction, while the right panel presents data from the out-of-plane [100] direction. At $T=5$ K for H parallel to the in-plane $[01\bar{1}]$ direction, we observe one resonance at $\mu_0H=236$ mT with a peak-to-peak linewidth of $\mu_0\Delta H_{pp}\approx36$ mT, while for H perpendicular to the sample surface ($H\|[100]$) there are three distinct resonances at $\mu_0H=576$, 492, and 430 mT, each with $\mu_0\Delta H_{pp}\approx25$ mT. With increasing temperature, the resonance fields for both orientations shift toward $\mu_0H=330$ mT, which corresponds to the resonance field of paramagnetic impurities with a g factor of $g=2$. The anisotropy disappears around $T\approx65$ K, slightly above the Curie temperature $T_C=55$ K determined from SQUID magnetization measurements. We attribute this to the moderately large applied field $\mu_0H\approx330$ mT in resonance, which stabilizes ferromagnetism even slightly above T_C (compare Fig. 3 in Ref. 9).

We attribute the multiple resonances in the $H\|[100]$ data to spin wave excitations.[25–28] Since we only observe three resonances or less, a detailed analysis of the mode spacing is hardly possible. However, assuming the resonance at the highest magnetic field $\mu_0H_0=576$ mT to be the collective mode, we determine a separation $\Sigma(n)=H_0-H_n\propto n^{0.8}$ between the resonance fields of the mode with the highest field H_0 and the nth spin wave mode H_n at $T=5$ K, which does not obey the classical behavior expected for a homogeneous film $\Sigma_{\text{classical}}(n)\propto n^2$.[26] We attribute this to the varying depth profile of the Mn concentration. A similar nonquadratic behavior of the mode spacing has been reported for $Ga_{1-x}Mn_xAs$ thin films exhibiting gradients in hole concentration.[25,27,28] Describing the implantation profile with a parabolic depth dependence of the Mn concentration, a linear modes spacing would be expected, in reasonable agreement with the observed behavior.

To elucidate the magnetic anisotropy of the samples we performed measurements of the angular dependence of the FMR for sample rotations in the (011) and (100) planes. The angular dependences of the resonance fields obtained at different temperatures are shown in Fig. 2. The panels on the left hand side correspond to rotations of the external magnetic field from the in-plane $[01\bar{1}]$ to the out-of-plane [100], and back to the in-plane $[0\bar{1}1]$ direction. For simplicity, we limit the discussion to the collective mode in the following. A uniaxial magnetic anisotropy with the magnetic hard axis perpendicular to the layer can be inferred from the increase in ferromagnetic resonance fields approaching [100]. Likewise, the fourfold symmetry observed for the in-plane rotations in the right hand panels demonstrates the presence of a cubic anisotropy contribution. Additionally, the fact that the $[01\bar{1}]$ and [011] orientations, as well as the [010] and [001] orientations are not degenerate indicates the contribution of further in-plane uniaxial anisotropy components.

For a quantitative simulation of these data we use the free energy density

$$\begin{aligned}F=&-MH(\sin\Theta\sin\Phi\sin\theta\sin\phi+\cos\Theta\cos\theta\\&+\sin\Theta\cos\Phi\sin\theta\cos\phi)+K_{\text{eff}}^{100}\sin^2\Theta\sin^2\Phi\\&-\frac{1}{2}K_{c1}^{\perp}\sin^4\Theta\sin^4\Phi-\frac{1}{2}K_{c1}^{\parallel}(\cos^4\Theta+\sin^4\Theta\cos^4\Phi)\\&+\frac{1}{2}K_u^{011}(\cos\Theta+\sin\Theta\cos\Phi)^2+K_u^{001}\sin^2\Theta\cos^2\Phi.\end{aligned}\tag{1}$$

The angles are given by the orientation of the saturation magnetization $M=M(\Theta,\Phi)$ and the magnetic field $H=H(\theta,\phi)$ (Fig. 3). The first term describes the Zeeman energy, while the second term represents an effective perpendicular uniaxial anisotropy K_{eff}^{100} and is composed of the sum of demagnetization and uniaxial magnetocrystalline components, $\frac{1}{2}\mu_0M^2$ and K_u^{100}, respectively. In order to describe the

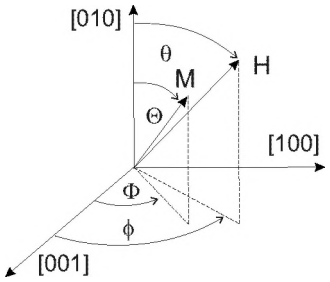

FIG. 3. Coordinate system used for FMR simulation, with the orientation of the saturation magnetization $M=M(\Theta,\Phi)$ and the magnetic field $H=H(\theta,\phi)$.

breaking of the cubic symmetry due to in-plane biaxial compressive strain induced by the presence of Mn, we include separate cubic terms for in-plane and perpendicular components, given by $K_{c1}^{\parallel}$ and $K_{c1}^{\perp}$, respectively. The in-plane cubic symmetry breaking is accounted for by the final two terms representing uniaxial contributions along [011] (K_u^{011}) and [001] (K_u^{001}). In all cases the appropriate anisotropy field is given by the ratio $2K/M$. The come about of the different anisotropy terms, as well as of the equivalence of first order cubic and second order uniaxial anisotropy, are discussed in Appendix A.

Following the approach of Smit *et al.*[29,30] we obtain the equation of motion

$$\left(\frac{\omega}{\gamma}\right)^2 = \frac{1}{M^2 \sin^2\Theta}\left[\left(\frac{\partial^2}{\partial\Phi^2}F\right)\left(\frac{\partial^2}{\partial\Theta^2}F\right) - \left(\frac{\partial}{\partial\Phi}\frac{\partial}{\partial\Theta}F\right)^2\right]_{\Phi_0,\Theta_0}, \tag{2}$$

with the gyromagnetic ratio $\gamma=\frac{g\mu_B}{\hbar}$, which has to be evaluated at the equilibrium orientation of the saturation magnetization determined from

$$\frac{\partial}{\partial\Phi}F\big|_{\Phi=\Phi_0} = \frac{\partial}{\partial\Theta}F\big|_{\Theta=\Theta_0} = 0. \tag{3}$$

The solution of these equations yields the FMR resonance condition. The full lines in Fig. 2 are simulations of the measured data with anisotropy fields plotted in Fig. 4. At 5 K, the results for four samples with $x=0.042$ are well reproducible, with $0.16\ \mathrm{T} < 2K_{\mathrm{eff}}^{100}/M < 0.19\ \mathrm{T}$, $-0.10\ \mathrm{T} < 2K_{c1}^{\perp}/M < -0.06\ \mathrm{T}$, $-0.04\ \mathrm{T} < 2K_{c1}^{\parallel}/M < -0.03\ \mathrm{T}$, $0\ \mathrm{T} < 2K_u^{011}/M < 0.012\ \mathrm{T}$, and $0\ \mathrm{T} < 2K_u^{001}/M < 0.02\ \mathrm{T}$. The magnetic anisotropy of these films is clearly dominated by the uniaxial and cubic contributions perpendicular to the film. The in-plane cubic and uniaxial anisotropies along [011] and [001] are all somewhat smaller. Figure 4 depicts the decrease of all of the anisotropy components with increasing temperature and demonstrates that all components disappear above the T_C of 55 K of the films as expected. As discussed above, only a small $2K_{\mathrm{eff}}^{100}/M$ is observed even above T_C at 65 K.

From SQUID magnetization measurements we estimate the saturation magnetization in the most heavily doped part of the film—i.e., near the peak of the Mn distribution—to $M=37$ kA/m. From this, we obtain an upper limit for the demagnetization field $\mu_0 M$ of 0.05 T. Therefore, the demagnetization field constitutes only about one fourth of the effective uniaxial magnetic anisotropy field along [100], $2K_{\mathrm{eff}}^{100}/M=0.19$ T, determined from the simulation of the angular dependence of FMR at 5 K. This strongly indicates the presence of a tetragonal distortion of the $Ga_{0.958}Mn_{0.042}P$ layer after pulsed-laser melting causing the dominating contribution K_u^{100} as in the case of $Ga_{1-x}Mn_xAs$, where a strong uniaxial magnetic anisotropy in the growth direction is commonly observed and is attributed to the tetragonal distortion of the $Ga_{1-x}Mn_xAs$ layer due to lattice-matched growth.[31–33] However, a quantitative detection of the distortion in case of $Ga_{0.958}Mn_{0.042}P$ via x-ray diffraction turns out to be difficult due to the inhomogeneous Mn profile after pulsed-laser melting and the accompanied broadening of the diffraction peaks.

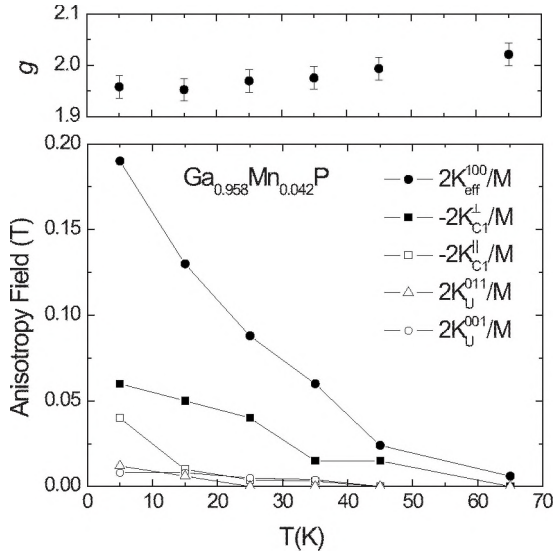

FIG. 4. Temperature dependence of the anisotropy parameters and the g factor obtained from the simulation of the angular dependence of the ferromagnetic resonance (full lines in Fig. 2).

One very interesting finding is that the magnetic easy axes of the in-plane cubic magnetic anisotropy are along $[01\bar{1}]$ and [011] directions as opposed to the [010] and [001] directions commonly observed for LT-MBE grown $Ga_{1-x}Mn_xAs$. This observation gives rise to the negative sign of $K_{c1}^{\parallel}$ in the $Ga_{0.958}Mn_{0.042}P$ samples studied ($K_{c1}^{\perp}$ is also negative). To the best of our knowledge, a negative cubic anisotropy has so far only been reported for $In_{1-x}Mn_xAs$.[34,35] Within the different models for carrier-mediated ferromagnetism in diluted magnetic semiconductors,[10,36] the sign of the cubic anisotropy is predicted to oscillate with varying hole concentration. However, the applicability of these models for the strongly localized, impurity-band-like character expected for the holes in $Ga_{1-x}Mn_xP$ remains an open question. Taking into account all anisotropy contributions, the global magnetic easy axis at 5 K is oriented close to the $[01\bar{1}]$ direction.

Interestingly, the g factor does not deviate significantly from $g=2$. In $Ga_{1-x}Mn_xAs$, g was found to be an effective g factor taking into account both the contributions of the Mn atoms and the hole subsystem.[37] Depending on the hole concentration p, Liu *et al.* observed a g factor at 4.2 K between $g=1.80$ for a sample with $p=1.64\times10^{20}$ cm^{-3} and $g=1.95$

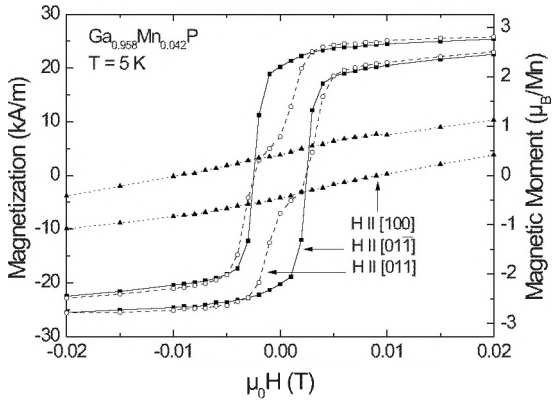

FIG. 5. $M(H)$ SQUID magnetization curves along the out-of-plane [100] (solid triangles) and the in-plane [01$\bar{1}$] (solid squares) and [011] (open circles) crystallographic axes. The lines are guides to the eye. The right and left vertical axes give the magnetic moment per *substitutional* Mn atom m_{Mn} and the magnetization M of the sample in the region of highest Mn concentration, respectively. These values were deduced from the measured total magnetic moment m_{tot} as described in Appendix B.

for a sample with $p=1.24\times10^{20}$ cm^{-3}.[37] The fact that g is found to vary from 1.95 to 2 for increasing temperature from 5 to 65 K indicates that there is only an even smaller contribution of the hole subsystem to the effective g factor in the case of $Ga_{1-x}Mn_xP$. This is consistent with the observations and calculations in Ref. 7 indicating a small hole concentration of up to 10^{20} cm^{-3}.

IV. SQUID MAGNETIZATION MEASUREMENTS

To substantiate the results obtained from FMR in the preceding section we also performed SQUID magnetization measurements. Figure 5 compares the $M(H)$ magnetization curves obtained at $T=5$ K for the external magnetic field oriented along the out-of-plane [100] (solid triangles) and the in-plane [01$\bar{1}$] (solid squares) and [011] (open circles) crystallographic axes. The squarelike $M(H)$ curve obtained for $H\|[01\bar{1}]$ also indicates that [01$\bar{1}$] is the easy magnetic axis at 5 K. Similarly, the large field of $\approx$0.2 T required to align M along the magnetically hard [100] direction is due to the large out-of-plane uniaxial and cubic anisotropy contributions. In the following, we use the free energy ansatz of Eq. (1) to simulate these $M(H)$ curves and especially to explain the kink observed for the magnetization measurement along [011].

To begin with, we focus on the $M(H)$ curve for $H\|[100]$ (out of plane) shown in Fig. 6(a) on a larger field scale. The dotted line is the curve simulated as discussed below for which we obtained the best agreement with the SQUID measurement using the anisotropy fields $2K_{\mathrm{eff}}^{100}/M=0.1$ T, $2K_{c1}^{\perp}/M=-0.12$ T, $2K_{c1}^{\parallel}/M=-0.04$ T, $2K_{u}^{011}/M=0.005$ T, and $2K_{u}^{001}/M=0.004$ T in Eq. (1). For $H\|[100]$ the simulated curve is predominantly determined by $2K_{\mathrm{eff}}^{100}/M$ and $2K_{c1}^{\perp}/M$. Both these parameters agree with the ones determined from FMR, to within a factor of two which can be understood as

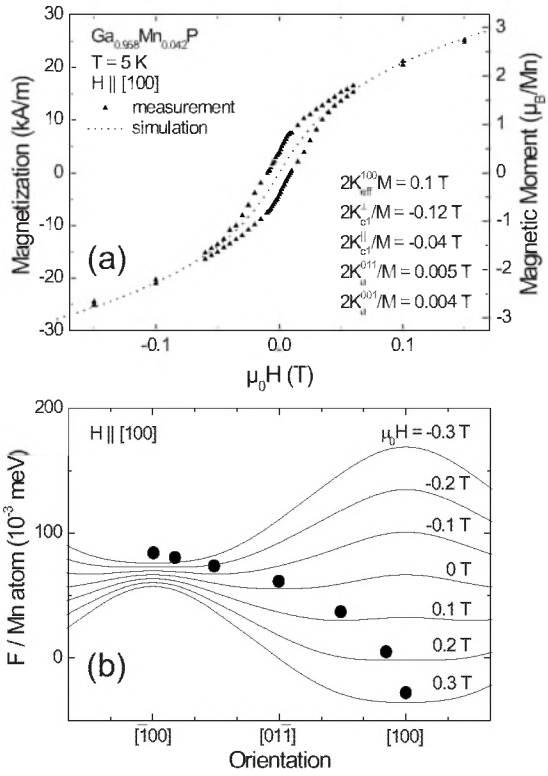

FIG. 6. (a) Comparison of the $M(H)$ SQUID magnetization curve measured for H along the out-of-plane [100] direction (full triangles) with the curve simulated using the anisotropy parameters given in the figure (dotted line). (b) Free energy per Mn atom as a function of the orientation of magnetization in the (011) plane for different magnetic fields applied along [100] calculated from Eq. (1). The position of the solid circle corresponds to the equilibrium orientation of magnetization in the minimum of the free energy surface. For clarity, the curves are shifted vertically.

follows. The FMR spectra for H oriented along the hard magnetic out-of-plane [100] axis features spin wave excitations. This not only indicates that there is a gradient in magnetic properties as already discussed above, but also that these modes are located at the region of the highest uniaxial anisotropy field $2K_{\mathrm{eff}}^{100}/M$ and therefore only probe the magnetic properties of this specific region. SQUID magnetization measurements in contrast integrate over the magnetic properties of the whole layer. In this respect the agreement of FMR and SQUID within a factor of two is quite reasonable.

The curvature of the simulated magnetization curve can be understood looking at the dependence of the free energy per Mn atom on the orientation of the magnetization in the (011) plane for different magnetic fields applied along [100] [Fig. 6(b)]. The position of the solid circle corresponds to the equilibrium orientation of magnetization in the minimum of the free energy surface. For high magnetic fields $H\|[100]$, the magnetization is also in the [100] direction, since then the Zeeman term is the dominant contribution in Eq. (1). This is the case for $\mu_0H=0.3$ T in Fig. 6(b). For decreasing magnetic fields the magnetocrystalline anisotropy becomes increasingly important. This leads to the migration of the minimum in the free energy surface—and therefore also equilibrium orientation of the magnetization—in the direc-

tion of the $[01\bar{1}]$ axis, which is the magnetic easy axis for the zero magnetic field. The application of a magnetic field in the opposite direction (i.e., $H\|[\bar{1}00]$) in turn tilts the magnetization more and more in this direction [Fig. 6(b)]. Having determined the orientation of the magnetization depending on the field strength H, we obtain the simulated curve in Fig. 6(a) via calculating the projection of the magnetization along the direction of the external magnetic field, which is the quantity measured by the SQUID magnetometer. The process of magnetization reversal described in this paragraph is called *coherent spin rotation*.[38]

For the simulation of the in-plane $M(H)$ curves in Fig. 7(a), in addition to coherent spin rotation, the process of *noncoherent spin switching* has to be considered following the discussion of Ref. 38. For $H\|[01\bar{1}]$, spin switching is visualized in Fig. 7(b), where the dependence of free energy per Mn atom on the orientation of the magnetization in the (100) film plane is plotted for different magnetic fields. Decreasing the external magnetic field $H\|[01\bar{1}]$ from its maximum value of 7 T to zero, the magnetization remains "trapped" in the global minimum at $[01\bar{1}]$. For negative fields, $[01\bar{1}]$ turns into a local minimum, while $[0\bar{1}1]$ becomes the global minimum in free energy. Since the thermal energy k_BT at $T=5$ K of 0.43 meV is three orders of magnitude larger than the energy needed to overcome the barrier between the two minima, there will always be some magnetic moments oriented along the direction of the global minimum. However, for the generation of a new magnetic domain with a magnetization along $[0\bar{1}1]$, the domain walls of the nucleus of this domain first have to be formed. The formation of these domain walls is energetically unfavorable, since the magnetic moments in the walls are oriented along the magnetic harder axes of the energy barriers. Therefore, magnetization reversal takes place only if the energy gain from tilting the magnetization into the direction of the global minimum accounts for the energy needed for the formation of the domain walls of this new magnetic domain. To obtain the experimentally observed switching field of −2.5 mT found for $M(H)$, with $H\|[01\bar{1}]$, we have to assume a domain wall formation energy of $\Delta E^{01\bar{1}}=8.6\times10^{-4}$ meV per Mn atom.

The situation for $H\|[011]$ is plotted in Fig. 7(c). Decreasing the external magnetic field $H\|[011]$ from its maximum value of 7 T to zero, the magnetization first also remains "trapped" in the global minimum at $[011]$. However, approaching $\mu_0H=0$ mT, $[01\bar{1}]$ becomes the global minimum due to the presence of the uniaxial anisotropy field along $[011]$. Therefore, there will be a first switching into the $[01\bar{1}]$ direction at positive fields and a second switching into the $[0\bar{1}\bar{1}]$ direction at large enough negative magnetic fields. In the model, we assumed the same energy barrier ΔE^{011} for both switching processes. Then, the parameters predominantly determining the switching fields are ΔE^{011} and $2K_u^{011}/M$. For increasing ΔE^{011} both switching processes occur later (at lower fields), while for increasing $2K_u^{011}/M$ the first switching process takes place earlier (at higher field) and

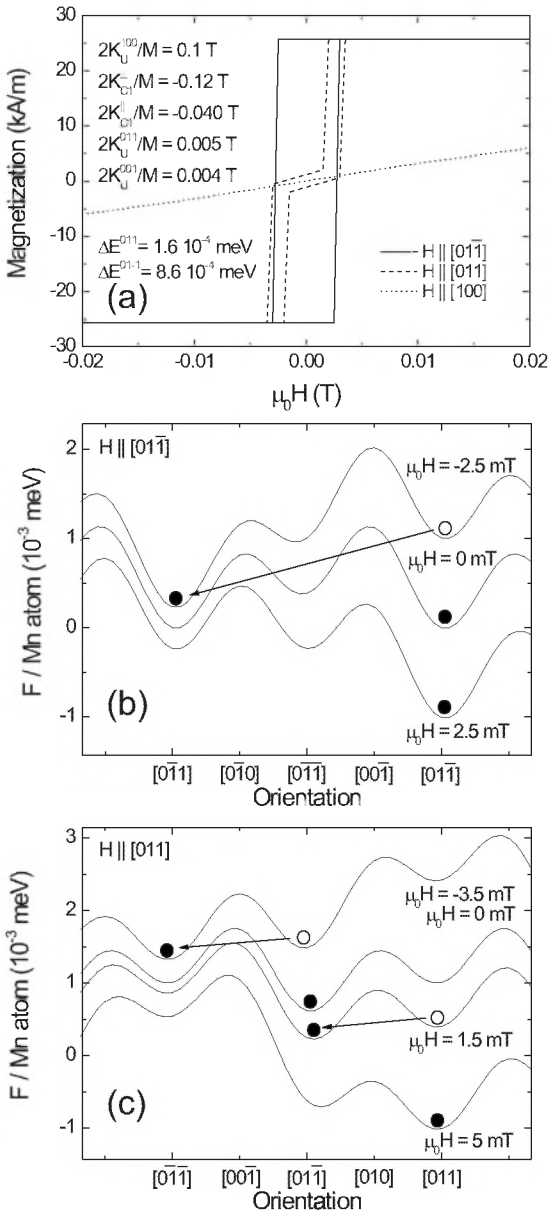

FIG. 7. (a) Simulated magnetization curves using the anisotropy parameters given in the figure. The solid, dashed, and dotted curves correspond to $H\|[01\bar{1}]$, $H\|[011]$, and $H\|[100]$, respectively. (b) Free energy per Mn atom as a function of the orientation of magnetization in the (100) film plane for different magnetic fields applied along $[01\bar{1}]$ and (c) along $[011]$. The position of the solid circle corresponds to the equilibrium orientation of magnetization in the minimum of the free energy surface. For clarity the curves are shifted vertically.

the second one later (at lower field). The best agreement with the experimentally observed switching fields, $\mu_0H=1.5$ mT for the first and $\mu_0H=-3.5$ mT for the second switching (compare Fig. 5), we obtained for the domain wall formation energy of $\Delta E^{011}=1.6\times10^{-4}$ meV per Mn atom and the uniaxial anisotropy field $2K_u^{011}/M=5$ mT. Note that in contrast to the 180° domain walls that must be formed in case of the magnetization reversal for $H\|[01\bar{1}]$, the domain walls that must be formed here comprise a 90° rotation of magne-

tization. Therefore it is not surprising that $\Delta E^{011} < \Delta E^{01\bar{1}}$. Typical values we obtain for the height of the energy barrier separating two local energy minima $\Delta F = 7 \times 10^{-4}$ meV per Mn ion are one order of magnitude smaller than the value obtained for a perpendicular magnetization-reversal process in the case of $Ga_{1-x}Mn_xAs$ by Liu *et al.*[38] Applying Kittel's Bloch domain wall model as discussed by Liu *et al.*[38] to our in-plane magnetization reversal process for $H \| [011]$, we obtain a size of a domain nucleus of approximately 5 μm. However, note that the assumption of a Bloch domain wall may not be justified in this case of an in-plane magnetized ferromagnetic film.

Consequently, the kink in the $M(H)$ curve for $H \| [011]$ can be explained by the fact that due to the presence of the uniaxial anisotropy field along [011], $[01\bar{1}]$ is not the global easy magnetic axis. At low fields a noncoherent spin switching into the global easy magnetic axis along $[01\bar{1}]$ takes place, which causes a vanishing projection of M on the [011] direction. The fact that there still is a finite projection in Fig. 7(a) is caused by the presence of the uniaxial in-plane anisotropy field $2K_u^{001}/M$ which slightly changes the 90° angle between the two minima of the cubic anisotropy near $[01\bar{1}]$ and [011].

It should be noted that our simulation only accounts for hysteresis effects caused by the noncoherent spin switching described above; the additional hysteresis effects observed, for example, for the $M(H)$ curve measured for H along the out-of-plane [100] direction are presumably caused by the pinning and depinning of domain walls at crystal defects, which is not included in our model. Furthermore, the magnetization is by far not saturated at magnetic fields of $\mu_0 H = 0.02$ T. Therefore, the saturation magnetization used in our model $M = 26$ kA/m is lower than the real saturation magnetization of $M = 37$ kA/m at $\mu_0 H = 7$ T. Internal stresses, or shape irregularities could explain the rounding of the magnetization curve at high fields.[39] However, in spite of the simplicity of the model, the $M(H)$ magnetization curves along several crystallographic directions can be explained at least semiquantitatively by the presence of the anisotropy fields determined from FMR.

Finally, we discuss the temperature dependence of magnetization along different crystallographic orientations (Fig. 8). In these measurements the sample is cooled down in the maximum available field $\mu_0 H_{cool} = 7$ T. At 5 K, the field is switched to $\mu_0 H_{measure} = 1$ mT and the projection of magnetization along the field direction is measured during warm up of the sample. For $H \| [01\bar{1}]$ (closed squares), we obtained the highest value for this projection at all temperatures in agreement with $[01\bar{1}]$ being the easy magnetic axis. Accordingly, the projection along [100] (closed triangles) is very small, since [100] is the hard magnetic axis. For $H \| [011]$ (open circles) and $T < 50$ K, the projection lies in between the values for the preceding orientations. This can be explained by the fact that [011] is not the global easy magnetic axis in this temperature range. Above 50 K, the curve for $H \| [011]$ overlaps with the one for $H \| [01\bar{1}]$, which is in good agreement with the disappearance of the uniaxial anisotropy field $2K_u^{011}/M$ in this temperature range (see Fig. 4), which lifts the degeneracy between the easy axes $[01\bar{1}]$ and [011]. Furthermore, the Curie temperature $T_C = 55$ K deduced from the $M(T)$ curves in Fig. 8 again nicely agrees with the temperature around which the anisotropy fields vanish in Fig. 4.

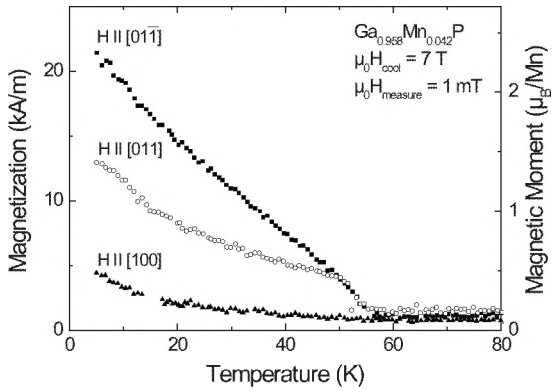

FIG. 8. Temperature dependence of magnetization for the sample cooled down to 5 K in a field of $\mu_0 H_{cool} = 7$ T and measured during warm up in a field of $\mu_0 H_{measure} = 1$ mT along the same crystallographic axis as in Fig. 5.

V. CONCLUSIONS

In conclusion, we have investigated the field and temperature dependencies of the magnetic anisotropy of $Ga_{0.958}Mn_{0.042}P$ thin films synthesized by ion implantation and pulsed laser melting using measurements of the angular dependence of both ferromagnetic resonance and SQUID magnetometry. The results of FMR and SQUID measurements including coherent spin rotation and noncoherent spin switching can be understood quantitatively using a relatively simple free energy model. Similar to $Ga_{1-x}Mn_xAs$ thin films, the magnetic anisotropy is dominated by a strong out-of-plane uniaxial contribution. Since the demagnetization field can only account for about one fourth of this out-of-plane uniaxial anisotropy field, its most probable origin is in-plane biaxial compressive strain, which is also the case for $Ga_{1-x}Mn_xAs$ thin films grown epitaxially on a GaAs substrate. We also observe a cubic anisotropy contribution. However, the sign of this cubic anisotropy term is opposite to the one commonly observed for $Ga_{1-x}Mn_xAs$. While the latter finding could still be in agreement with Dietl's theory of hole-mediated ferromagnetism considering the significantly reduced hole concentration in $Ga_{1-x}Mn_xP$ compared to $Ga_{1-x}Mn_xAs$, it remains to be demonstrated that this theory can indeed be applied to material systems exhibiting highly localized holes such as $Ga_{1-x}Mn_xP$. Nevertheless, it is a very interesting observation that in spite of the highly localized character of the holes in $Ga_{1-x}Mn_xP$, all the magnetic properties (saturation magnetization, absolute values of the anisotropy fields, Curie temperature) are similar to those typically observed in $Ga_{1-x}Mn_xAs$. This constitutes an important constraint for theories attempting to explain carrier-mediated ferromagnetism in highly localized material systems. Finally, the observation of symmetry-breaking in-plane uniaxial anisotropy components similar to that seen in

$Ga_{1-x}Mn_xAs$—where the origin still is under debate—indicates an intrinsic origin related to the hole-mediated ferromagnetic phase in III-Mn-V ferromagnetic semiconductors. Moreover, because our samples were fabricated via II-PLM—a form of liquid-phase epitaxy—explanations brought forward that invoke vapor phase growth processes including effects of surface reconstruction can be excluded as the origin of this in-plane symmetry breaking.

ACKNOWLEDGMENTS

We thank E. E. Haller for use of the ion implantation facilities and I. D. Sharp and J. W. Beeman for experimental assistance. The work at the Walter Schottky Institut was supported by Deutsche Forschungsgemeinschaft through SFB 631 and the Bavaria California Technology Center. The work at Berkeley was supported by the Director, Office of Science, Office of Basic Energy Sciences, Division of Materials Sciences and Engineering, of the U.S. Department of Energy under Contract No. DEAC02-05CH11231 and previous contracts.

APPENDIX A: ANISOTROPY ENERGY

Magnetic anisotropy can, e.g., be caused by dipole-dipole interaction, crystal fields, and spin-orbit coupling. Furthermore, uniaxial and biaxial strain can be an origin for magnetic anisotropies. While to date no comprehensive *ab initio* understanding of magnetic anisotropy has been established, magnetic anisotropy can be efficiently described mathematically with the help of symmetry considerations. According to Chikazumi,[40] the free energy of a uniaxial anisotropy can be expressed by expanding it in a series of powers of $\sin^2\vartheta$,

$$F_u = \tilde{K}_{u1}\sin^2\vartheta + \tilde{K}_{u2}\sin^4\vartheta + \cdots , \tag{A1}$$

with the first- and second-order constants $\tilde{K}_{u1}$ and $\tilde{K}_{u2}$, respectively, and the angle ϑ between the orientation of magnetization $\vec{m}=\frac{\vec{M}}{M}$ and the anisotropy axis $\vec{u}$. This can be rewritten using $\sin^2\vartheta = 1-\cos^2\vartheta$, so that

$$\begin{aligned} F_u &= \tilde{K}_{u1}(1-\cos^2\vartheta) + \tilde{K}_{u2}(1-\cos^2\vartheta)^2 + \cdots \\ &= (\tilde{K}_{u1}+\tilde{K}_{u2}) + (-\tilde{K}_{u1}-2\tilde{K}_{u2})\cos^2\vartheta + \tilde{K}_{u2}\cos^4\vartheta + \cdots \\ &= \text{const} + K_{u1}\cos^2\vartheta + K_{u2}\cos^4\vartheta + \cdots , \end{aligned} \tag{A2}$$

with $K_{u1} := -\tilde{K}_{u1} - 2\tilde{K}_{u2}$ and $K_{u2} := \tilde{K}_{u2}$. Using

$$\vec{m} = \frac{\vec{M}}{M} = \begin{pmatrix} \alpha_x \\ \alpha_y \\ \alpha_z \end{pmatrix}$$

with the direction cosines of the Cartesian axes $\alpha_x = \sin\Theta\sin\Phi$, $\alpha_y = \cos\Theta$, and $\alpha_z = \sin\Theta\cos\Phi$ from Fig. 3, the first-order uniaxial anisotropy contribution along

$$\vec{u} = \frac{1}{\sqrt{2}}\begin{pmatrix} 0 \\ 1 \\ 1 \end{pmatrix}$$

in Eq. (1), for example, is obtained via

$$F_u^{011} = K_u^{011}(\vec{m}\vec{u})^2 = \frac{1}{2}K_u^{011}(\cos\Theta + \sin\Theta\cos\Phi)^2. \tag{A3}$$

The free energy for cubic magnetocrystalline anisotropy in cubic systems according to Chikazumi[40] is given by

$$F_c = K_{c1}(\alpha_x^2\alpha_y^2 + \alpha_y^2\alpha_z^2 + \alpha_z^2\alpha_x^2) + K_{c2}\alpha_x^2\alpha_y^2\alpha_z^2 + \cdots . \tag{A4}$$

With the addition theorem for the direction cosines

$$\alpha_x^4 + \alpha_y^4 + \alpha_z^4 = 1 - 2(\alpha_x^2\alpha_y^2 + \alpha_y^2\alpha_z^2 + \alpha_z^2\alpha_x^2), \tag{A5}$$

Eq. (A4) can be transferred to

$$F_c = \text{const} - \frac{1}{2}K_{c1}(\alpha_x^4 + \alpha_y^4 + \alpha_z^4) + K_{c2}\alpha_x^2\alpha_y^2\alpha_z^2 + \cdots . \tag{A6}$$

Therefore, the α_i^4 terms in Eq. (A6) link the first-order cubic anisotropy and the second-order uniaxial anisotropy given in Eq. (A2). Consequently, the latter formulation for first-order cubic anisotropy is equivalent to a linear combination of second-order uniaxial anisotropies along the Cartesian axes, $F_{u2}^i = K_{u2}^i\alpha_i^4$, $i \in \{x,y,z\}$.

In Eq. (1) we accounted for the tetragonal crystal symmetry via distinguishing in-plane and out-of-plane cubic anisotropies. Following the above discussion one could equivalently use a combination of a first-order cubic anisotropy and a second-order uniaxial anisotropy perpendicular to the film plane

$$-\frac{1}{2}K_{c1}^{\perp}\alpha_x^4 - \frac{1}{2}K_{c1}^{\parallel}(\alpha_y^4 + \alpha_z^4) = -\frac{1}{2}K_{c1}(\alpha_x^4 + \alpha_y^4 + \alpha_z^4) + K_{u2}^{100}\alpha_x^4, \tag{A7}$$

with the first-order cubic anisotropy constant $K_{c1} = K_{c1}^{\parallel}$ and the second-order uniaxial anisotropy constant perpendicular to the film plane $K_{u2}^{100} = -\frac{1}{2}(K_{c1}^{\perp} - K_{c1}^{\parallel})$.

Note also that because of

$$\alpha_x^2 + \alpha_y^2 + \alpha_z^2 = 1, \tag{A8}$$

only two of the three first-order uniaxial anisotropy constants K_{u1}^{100}, K_{u1}^{010}, and K_{u1}^{001} are independent. A first-order uniaxial anisotropy can always be expressed by two other first-order uniaxial anisotropies perpendicular to each other. Analogously, the second-order uniaxial anisotropy constants also are not independent because of Eq. (A5).

APPENDIX B: DETERMINATION OF MAGNETIZATION

Due to the Mn implantation profile, the magnetization cannot be calculated as usual via dividing the total magnetic moment m_{tot} measured, e.g., via SQUID magnetometry by the sample volume. In a first step we calculate the magnetic moment per *substitutional* Mn atom via

$$m_{\mathrm{Mn}} = \frac{m_{\mathrm{tot}}}{D_{\mathrm{Mn,retained}} A f_{\mathrm{subst}}}, \tag{B1}$$

where $D_{\mathrm{Mn,retained}} = 7.3 \times 10^{15}$ cm^{-2} is the Mn implantation dose retained after II-PLM, A is the sample area, and $f_{\mathrm{subst}} = 0.7$ is the fraction of substitutional Mn atoms derived via RBS and PIXE. To obtain an estimate for the magnetization of the sample in the region of highest Mn concentration we multiply the average magnetic moment per Mn atom with the peak substitutional Mn concentration x and the density of Ga lattice sites $[\mathrm{Ga}] = 2.47 \times 10^{22}$ cm^{-3},

$$M = m_{\mathrm{Mn}} x [\mathrm{Ga}]. \tag{B2}$$

*bihler@wsi.tum.de
†Present address: Materials Department, University of California, Santa Barbara, CA 93106, USA. mikes@engineering.ucsb.edu

[1] A. M. Nazmul, S. Sugahara, and M. Tanaka, Phys. Rev. B **67**, 241308(R) (2003).
[2] K. W. Edmonds, P. Bogusławski, K. Y. Wang, R. P. Campion, S. N. Novikov, N. R. S. Farley, B. L. Gallagher, C. T. Foxon, M. Sawicki, T. Dietl, M. Buongiorno Nardelli, and J. Bernholc, Phys. Rev. Lett. **92**, 037201 (2004).
[3] C. Jaeger, C. Bihler, T. Vallaitis, S. T. B. Goennenwein, M. Opel, R. Gross, and M. S. Brandt, Phys. Rev. B **74**, 045330 (2006).
[4] T. Graf, S. T. B. Goennenwein, and M. S. Brandt, Phys. Status Solidi B **239**, 277 (2003).
[5] E. Sarigiannidou, F. Wilhelm, E. Monroy, R. M. Galera, E. Bellet-Amalric, A. Rogalev, J. Goulon, J. Cibert, and H. Mariette, Phys. Rev. B **74**, 041306(R) (2006).
[6] M. A. Scarpulla, B. L. Cardozo, R. Farshchi, W. M. Hlaing Oo, M. D. McCluskey, K. M. Yu, and O. D. Dubon, Phys. Rev. Lett. **95**, 207204 (2005).
[7] R. Farshchi, M. A. Scarpulla, P. R. Stone, K. M. Yu, I. D. Sharp, J. W. Beeman, H. H. Silvestri, L. A. Reichertz, E. E. Haller, and O. D. Dubon, Solid State Commun. **140**, 443 (2006).
[8] P. R. Stone, M. A. Scarpulla, R. Farshchi, I. D. Sharp, J. W. Beeman, K. M. Yu, E. Arenholz, J. D. Denlinger, E. E. Haller, and O. D. Dubon, AIP Conf. Proc. **893**, 1177 (2007).
[9] P. R. Stone, M. A. Scarpulla, R. Farshchi, I. D. Sharp, E. E. Haller, O. D. Dubon, K. M. Yu, J. W. Beeman, E. Arenholz, J. D. Denlinger, and H. Ohldag, Appl. Phys. Lett. **89**, 012504 (2006).
[10] T. Dietl, H. Ohno, and F. Matsukura, Phys. Rev. B **63**, 195205 (2001).
[11] T. Dietl, H. Ohno, F. Matsukura, J. Cibert, and D. Ferrand, Science **287**, 1019 (2000).
[12] H. Kepa, L. Van Khoi, C. M. Brown, T. Dietl, J. K. Furdyna, and T. M. Giebultowicz, Physica B **350**, 36 (2004).
[13] A. Kaminski and S. Das Sarma, Phys. Rev. Lett. **88**, 247202 (2002).
[14] A. C. Durst, R. N. Bhatt, and P. A. Wolff, Phys. Rev. B **65**, 235205 (2002).
[15] K. Hirakawa, A. Oiwa, and H. Munekata, Physica E (Amsterdam) **10**, 215 (2001).
[16] E. J. Singley, R. Kawakami, D. D. Awschalom, and D. N. Basov, Phys. Rev. Lett. **89**, 097203 (2002).
[17] P. Mahadevan and A. Zunger, Appl. Phys. Lett. **85**, 2860 (2004).
[18] K. Sato, P. H. Dederichs, H. Katayama-Yoshida, and J. Kudrnovský, J. Magn. Magn. Mater. **272-276**, 1983 (2004).
[19] T. Jungwirth, J. Sinova, J. Mašek, J. Kučera, and A. H. MacDonald, Rev. Mod. Phys. **78**, 809 (2006).
[20] H. Katayama-Yoshida, K. Sato, T. Fukushima, M. Toyoda, H. Kizaki, V. A. Dinh, and P. H. Dederichs, Phys. Status Solidi A **204**, 15 (2007).
[21] J. Masek, J. Kudrnovský, F. Máca, J. Sinova, A. H. MacDonald, R. P. Campion, B. L. Gallagher, and T. Jungwirth, Phys. Rev. B **75**, 045202 (2007).
[22] M. A. Scarpulla, O. D. Dubon, K. M. Yu, O. Monteiro, M. R. Pillai, M. J. Aziz, and M. C. Ridgway, Appl. Phys. Lett. **82**, 1251 (2003).
[23] O. D. Dubon, M. A. Scarpulla, R. Farshchi, and K. M. Yu, Physica B **376-377**, 630 (2006).
[24] K. M. Yu, W. Walukiewicz, T. Wojtowicz, I. Kuryliszyn, X. Liu, Y. Sasaki, and J. K. Furdyna, Phys. Rev. B **65**, 201303(R) (2002).
[25] S. T. B. Goennenwein, T. Graf, T. Wassner, M. S. Brandt, M. Stutzmann, J. B. Philipp, R. Gross, M. Krieger, K. Zuern, P. Ziemann, A. Koeder, S. Frank, W. Schoch, and A. Waag, Appl. Phys. Lett. **82**, 730 (2003).
[26] C. Kittel, Phys. Rev. **110**, 1295 (1958).
[27] A. Koeder, S. Frank, W. Schoch, V. Avrutin, W. Limmer, K. Thonke, R. Sauer, A. Waag, M. Krieger, K. Zuern, P. Ziemann, S. Brotzmann, and H. Bracht, Appl. Phys. Lett. **82**, 3278 (2003).
[28] T. G. Rappoport, P. Redlinski, X. Liu, G. Zarand, J. K. Furdyna, and B. Janko, Phys. Rev. B **69**, 125213 (2004).
[29] J. Smit and H. P. J. Wijn, Adv. Electron. Electron Phys. **6**, 70 (1954).
[30] J. Smit and H. G. Beljers, Philips Res. Rep. **10**, 113 (1955).
[31] X. Liu, Y. Sasaki, and J. K. Furdyna, Phys. Rev. B **67**, 205204 (2003).
[32] C. Bihler, H. Huebl, M. S. Brandt, S. T. B. Goennenwein, M. Reinwald, U. Wurstbauer, M. Döppe, D. Weiss, and W. Wegscheider, Appl. Phys. Lett. **89**, 012507 (2006).
[33] W. Limmer, M. Glunk, J. Daeubler, T. Hummel, W. Schoch, R. Sauer, C. Bihler, H. Huebl, M. S. Brandt, and S. T. B. Goennenwein, Phys. Rev. B **74**, 205205 (2006).
[34] X. Liu, W. Lim, Z. Ge, S. Shen, M. Dobrowolska, J. Furdyna, T. Wojtowicz, K. Yu, and W. Walukiewicz, Appl. Phys. Lett. **86**, 112512 (2005).
[35] M. Sawicki, F. Matsukura, A. Idziaszek, T. Dietl, G. M. Schott, C. Ruester, C. Gould, G. Karczewski, G. Schmidt, and L. W. Molenkamp, Phys. Rev. B **70**, 245325 (2004).
[36] M. Abolfath, T. Jungwirth, J. Brum, and A. H. MacDonald, Phys. Rev. B **63**, 054418 (2001).
[37] X. Liu, W. L. Lim, M. Dobrowolska, J. K. Furdyna, and T. Wojtowicz, Phys. Rev. B **71**, 035307 (2005).
[38] X. Liu, W. L. Lim, L. V. Titova, M. Dobrowolska, J. K. Furdyna, M. Kutrowski, and T. Wojtowicz, J. Appl. Phys. **98**, 063904 (2005).
[39] A. Hubert and R. Schäfer, *Magnetic Domains* (Springer, Berlin, 1998).
[40] S. Chikazumi, *Physics of Magnetism* (John Wiley & Sons, New York, 1964).